

ELECTROCHEMISTRY

Fluorinated solid electrolyte interphase enables highly reversible solid-state Li metal battery

Xiulin Fan^{1,2*}, Xiao Ji^{2,3*}, Fudong Han², Jie Yue², Ji Chen², Long Chen², Tao Deng², Jianjun Jiang³, Chunsheng Wang^{2†}

Solid-state electrolytes (SSEs) are receiving great interest because their high mechanical strength and transference number could potentially suppress Li dendrites and their high electrochemical stability allows the use of high-voltage cathodes, which enhances the energy density and safety of batteries. However, the much lower critical current density and easier Li dendrite propagation in SSEs than in nonaqueous liquid electrolytes hindered their possible applications. Herein, we successfully suppressed Li dendrite growth in SSEs by in situ forming an LiF-rich solid electrolyte interphase (SEI) between the SSEs and the Li metal. The LiF-rich SEI successfully suppresses the penetration of Li dendrites into SSEs, while the low electronic conductivity and the intrinsic electrochemical stability of LiF block side reactions between the SSEs and Li. The LiF-rich SEI enhances the room temperature critical current density of Li_3PS_4 to a record-high value of $>2 \text{ mA cm}^{-2}$. Moreover, the Li plating/stripping Coulombic efficiency was escalated from 88% of pristine Li_3PS_4 to more than 98% for LiF-coated Li_3PS_4 . In situ formation of electronic insulating LiF-rich SEI provides an effective way to prevent Li dendrites in the SSEs, constituting a substantial leap toward the practical applications of next-generation high-energy solid-state Li metal batteries.

INTRODUCTION

The lithium ion battery (LIB) is undoubtedly one of the landmark energy storage technologies that have significantly altered our lives, owing to its much higher energy density and reversibility than any other secondary batteries (1). Recently, LIBs have penetrated from consumer electronics to large-scale energy storage, including in the automotive industry and in grid-scale stationary energy storage. However, as the electric vehicle market rapidly expands, the energy density of the LIBs based on the intercalation chemistries becomes a bottleneck, limiting the driving range of the vehicles (1). Therefore, new battery chemistries using high-capacity Li metal anodes and high-energy cathodes are urgently desired (2, 3). On the other hand, almost all of these commercialized LIBs are based on the highly flammable and fluid carbonate electrolytes, which induced serious safety issues under harsh working conditions.

Inorganic solid-state batteries have emerged as very attractive alternatives to these commercial liquid electrolyte batteries (4) because of their enhanced safety, wide operating temperature range, and potentially high energy densities, especially when coupled with the Li metal as the anode (4). Solid-state electrolytes (SSEs) have been regarded as ideal electrolytes to physically curb the growth of the Li dendrites and eliminate irreversible electrolyte consumption (5). According to the stability criterion proposed by Monroe and Newman (6), almost all of the promising SSEs, such as Li_3PS_4 (LPS), $\text{Li}_{10}\text{GeP}_2\text{S}_{12}$ (LGPS), $\text{Li}_{3x}\text{La}_{2/3-x}\text{TiO}_3$ (LLTO), $\text{Li}_7\text{La}_3\text{Zr}_2\text{O}_{12}$ (LLZO), and their related derivatives, should be able to prevent Li dendrite formation because of their high mechanical strength (7). Moreover, the Sand's time (the starting time for the Li dendrite initiation) of the SSEs should be infinite since their Li^+ transference numbers are

approaching to 1 (8). However, rather than suppressing the Li dendrites, SSEs actually prompt Li dendrite growth, as evidenced by the much lower critical current densities (at which an Li dendrite forms) than those in the nonaqueous liquid electrolytes (9–11). Almost all reported critical current densities in SSEs are $<1 \text{ mA cm}^{-2}$ (9, 11–17), which is less than $1/10$ of that in the ether-based electrolytes (18) and $1/5$ of that in the carbonate-based electrolytes (19, 20). Even worse, Chiang and colleagues (9) recently demonstrated that the Li dendrites could readily penetrate all the SSEs (sulfides and oxides) with a much lower current density, no matter whether they are polycrystalline, single crystalline, amorphous, or polished with limited surface defects.

The mechanisms for Li dendrite propagation in SSEs are still not fully understood, not to mention the approaches to suppress the dendrites in the SSEs. Yet, a consensus steered by the recent advances is that all of these state-of-the-art SSEs (such as LPS, LGPS, LLTO, and LLZO) are thermodynamically not stable to the Li metal (21–24). If the ingredient nonuniformity in the grain boundaries and the negative potentials ($<0.0 \text{ V}$ versus Li^+/Li depending on the Li plating currents) at the Li-SSE interface due to the Li plating overpotential are considered, more prominent parasitic reactions will take place, forming an interphase layer. The nature of the interphase layer plays a pivotal role in the Li dendrite formation and growth in the SSEs. For example, the electronic conductive interphase layers formed by reacting Li with a coating layer cannot suppress the Li dendrite formation (25).

In the present paper, we demonstrated that a thin LiF-rich solid electrolyte interphase (SEI) layer with a high interfacial energy to Li metal and low electronic conductivity can effectively suppress Li dendrite formation and prevent side reactions between the Li and LPS, thus enhancing the critical current density from 0.7 mA cm^{-2} for pristine LPS to a record-high value of $>2 \text{ mA cm}^{-2}$ for the LiF-rich SEI-coated SSE. LiF-rich SEIs also enhanced the Li plating/stripping Coulombic efficiency (CE) from ~ 88 to $\sim 98\%$. The LiF-rich SEI is simply formed by contacting Li with LiFSI-coated/infiltrated LPS. Different from the reported surface wetting layers and the buffer layers, formation of an SEI between the SSE and the Li anode that has high interface energy with Li and strong modulus provides novel ways to

Copyright © 2018
The Authors, some
rights reserved;
exclusive licensee
American Association
for the Advancement
of Science. No claim to
original U.S. Government
Works. Distributed
under a Creative
Commons Attribution
NonCommercial
License 4.0 (CC BY-NC).

¹School of Materials Science and Engineering, Zhejiang University, Hangzhou 310027, PR China. ²Department of Chemical and Biomolecular Engineering, University of Maryland, College Park, MD 20740, USA. ³School of Optical and Electronic Information, Huazhong University of Science and Technology, Wuhan, Hubei 430074, PR China.

*These authors contributed equally to this work.

†Corresponding author. Email: cswang@umd.edu

suppress the Li dendrite in the SSEs and paves the way for next-generation high-energy solid-state Li metal batteries.

RESULTS

Electrochemical performance

Inspired by the significant success in SEI design to suppress Li dendrite and prevent side reactions in the nonaqueous liquid electrolytes (2, 18, 19, 26), constructing a robust SEI layer between the solid electrolytes and the Li metal anodes should be the most efficient approach to inhibit the side reactions between the electrolytes and Li metal and meanwhile suppress the Li dendrite generation (19). In our design, a thin uniform LiF-rich SEI layer was formed in situ between the LiFSI-coated/infiltrated LPS and the Li metal anode. Figure 1A schematically depicts the configuration of the LiF-rich SEI layer between the Li metal and the LPS SSE. A drop of highly concentrated 6 M LiFSI dimethoxyethane (DME) ($\sim 20\ \mu\text{l}$) was infiltrated between the Li metal anode and the LPS SSE and then dried under vacuum at 120°C overnight to evaporate the DME solvent. During the evacuation and the following Li plating/stripping process, an LiF-rich SEI will be conformably formed between the SSE and the Li metal anode due to the reaction of the LiFSI with the Li metal (19). LiFSI has a much lower lowest unoccupied molecular orbital energy ($-1.70\ \text{eV}$) (19) than that of the DME ($1.6\ \text{eV}$) (27), implying that LiFSI has a high tendency to react with the Li metal, especially at an elevated temperature of 120°C . In addition, the reaction rate of the $-\text{SO}_2\text{F}$ group in LiFSI to the Li metal is very fast (19). The S-F bond will first be broken to form a stable LiF layer on the Li metal surface, and then the breakage of N-S bond and other decomposed segments of FSI⁻ leads to the generation of SO_2 , which will evaporate as gas (19). Therefore, an LiF-rich SEI is eventually formed at the Li metal surface. In addition, the infiltrated LiFSI inside the LPS can also consume the Li dendrites even if they penetrate into the LPS through LiF-rich SEI.

An x-ray diffraction (XRD) pattern in fig. S1A shows that the ball-milled LPS SSE has an amorphous structure. The Li ion conductivity calculated from the impedance spectra (fig. S1B) is about $2.6 \times 10^{-4}\ \text{S cm}^{-1}$ at room temperature, which is comparable to the previously reported values (12). The dendrite-suppressing ability of LiFSI@ Li_3PS_4 SSE and pristine LPS SSE was evaluated at room temperature (25°C) using symmetric Li|LiFSI@LPS|Li and Li|LPS|Li cells, respectively. Figure 2 (A and B) shows the voltage profiles of two symmetric cells during Li plating and stripping at a fixed capacity of $0.1\ \text{mAh cm}^{-2}$ but a step-increased current density. Initially, both cells showed a similar increase in Li plating/stripping overpotentials with the increment of the current density. As the

current density increased to $0.7\ \text{mA cm}^{-2}$, a sudden voltage drop was observed at the seventh cycle in the Li|LPS|Li cell because of the dendrite penetration into the SSE. The critical current density of $0.7\ \text{mA cm}^{-2}$ is in the range of the previously reported value (0.5 to $1.0\ \text{mA cm}^{-2}$) (10). Conversely, no voltage drop could be observed for the Li|LiFSI@LPS|Li cell even as the current density was increased to over $2\ \text{mA cm}^{-2}$. These results clearly demonstrate that the in situ-formed LiF-rich SEI layer between the LPS SSE and the Li metal can significantly increase the critical current density and suppress the Li dendrites. Although the bulk LiF is a poor Li^+ conductor, the in situ-formed thin LiF-rich SEI layer does not reduce the ion transport kinetics, which was proved by the similar overpotentials of Li plating/stripping in the two symmetric cells (Li|LiFSI@LPS|Li and Li|LPS|Li) before the short circuit of the LiF-free cell (Fig. 2, A and B). The low resistance of LiF-rich SEI is because (i) the in situ-formed thin SEI is tightly contacted with both Li and LPS and (ii) the much lower energy barrier for Li^+ surface diffusion on LiF ($0.17\ \text{eV}$ for LiF and $0.23\ \text{eV}$ for Li_2CO_3) (28, 29) promotes Li^+ migration along the LiF surface rather than the dendritic plating. In contrast, because of the higher Li^+ surface diffusion barrier energy at the Li_2CO_3 surface, Li_2CO_3 cannot inhibit the Li dendrite formation (28, 29).

Cycling performances of the two symmetric Li|LiFSI@LPS|Li and Li|LPS|Li cells were compared at a current density of $0.3\ \text{mA cm}^{-2}$ at room temperature. As shown in Fig. 2C, the Li|LPS|Li cell can only stably charge/discharge for 60 hours, and then a gradual decrease in the voltage was observed because of the progressive dendrite penetration into the LPS SSE. After about 90 hours of cycling, a sudden voltage drop due to the completely short circuit was detected, as confirmed by the electrochemical impedance spectroscopy (EIS) results (fig. S2). The fluctuating and irregular voltage variations after the short circuit suggest the serious parasitic reactions between the SSE and the penetrated Li dendrites, generating a nonzero resistance of the dendrites (12). The Li|LiFSI@LPS|Li cell with an LiF-rich SEI layer between the Li metal and the SSE showed much stable Li plating/stripping profiles for over 300 hours without any short circuit (Fig. 2D and fig. S3).

In contrast to forming SEI between Li and solid electrolytes, electronic conducting (such as Au, Si, and Ge) layers between Li and solid electrolytes are also reported to enhance the Li wettability to solid electrolyte, thus suppressing the Li dendrites. Since CE is a sensitive indicator for Li dendrite growth and stability between the electrolyte and the Li metal, the CEs for Li plating/stripping in three LPS electrolytes (LiFSI-coated/infiltrated LPS, Au-coated LPS, and pristine LPS electrolytes) were evaluated using Swagelok SS|electrolyte|Li half cells where stainless steel (SS) served as a current collector. Au-coated LPS was prepared by coating a 10-nm layer of Au on both sides of the LPS electrolyte surface. Similar CE of 86 to 90% was obtained for both SS|LPS|Li and SS|Au@LPS|Li cells (Fig. 3, A and B), indicating that the Au coating cannot block the parasitic reactions between the SSE and the Li metal, although the Li plating/stripping polarization was reduced because of the enhancement of the contact areas between the LPS and the Li metal (Fig. 3B). For the Au-coated LPS electrolyte, once the Au contacts with the Li metal, it will instantly form the fully lithiated $\text{Li}_{15}\text{Au}_4$ phase. This highly conductive alloy layer tightly adhering to the Li metal has the same potential as the Li metal. Although a better contact between LPS and Li reduces the Li plating/stripping overpotentials, it cannot block any side reactions between the SSEs and the Li metal anode. It should be pointed out that recently, Sakamoto and colleagues also found that the Au interlayer could not

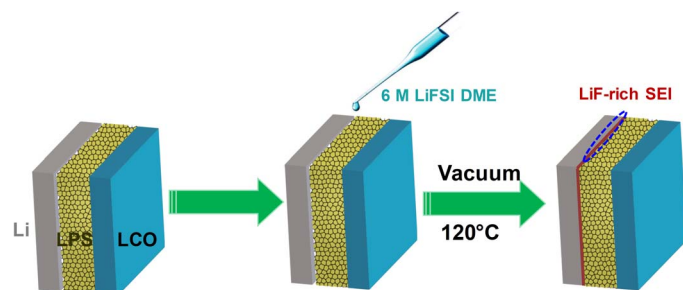


Fig. 1. Schematic illustration of the pretreated processes for the formation of an LiF-rich SEI layer between the Li metal and the LPS SSEs.

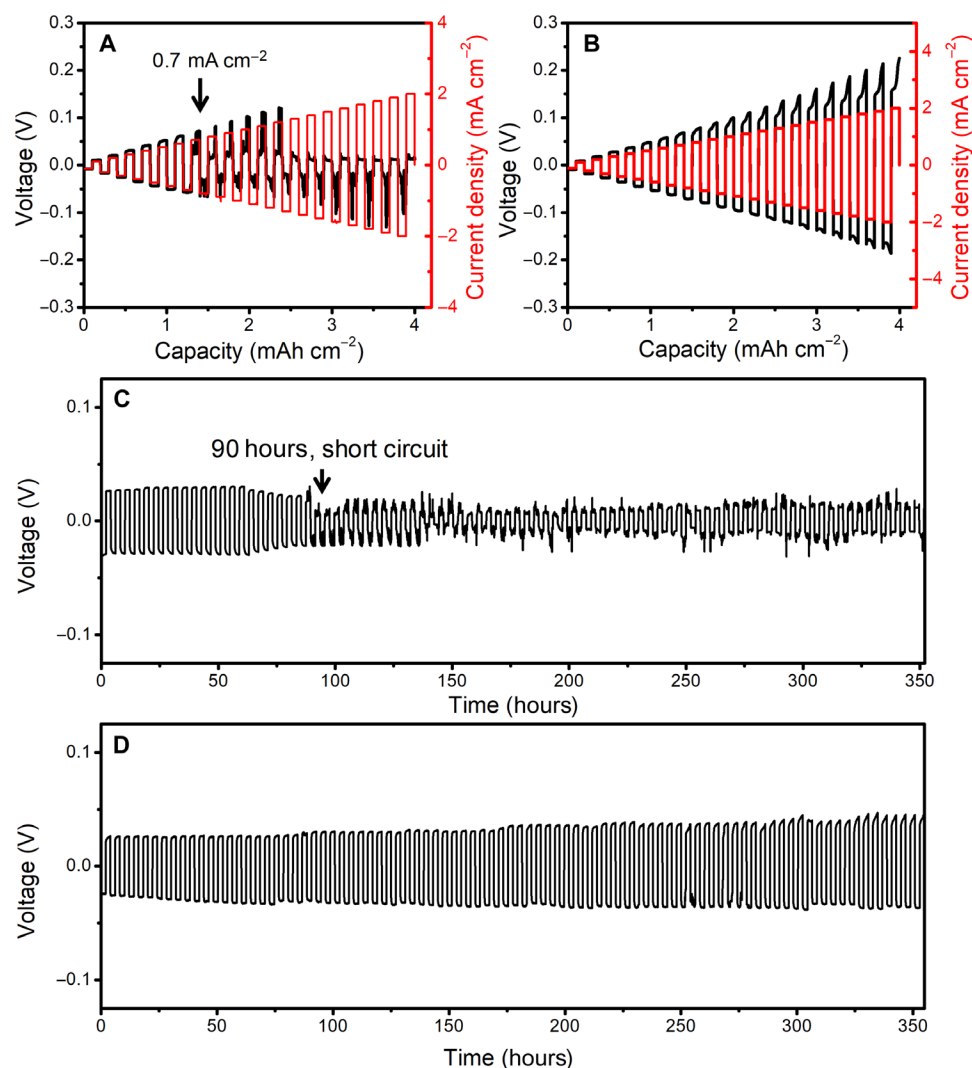


Fig. 2. Electrochemical performances of the Li plating/stripping in the Li|LiFSI@LPS|Li cell and the Li|LPS|Li cell. Galvanostatic Li plating/stripping profiles in the Li|LPS|Li cell (A) and the Li|LiFSI@LPS|Li cell (B) at step-increased current densities. Galvanostatic cycling of Li plating/stripping profiles in the Li|LPS|Li cell (C) and the Li|LiFSI@LPS|Li cell (D) at a constant current density of 0.3 mA cm⁻². All tests were performed at room temperature (25°C).

increase the critical current density in the LLZO garnet SSE system either (25). For the LiFSI-treated LPS cell, residual LiFSI will react with the deposited Li metal to form an LiF-rich SEI in the initial Li plating process, resulting in an initial CE of 72%, which is lower than the CE of the untreated LPS cell (86%) or the Au-coated LPS cell (88%). However, after several activation cycles, the CE for LiFSI-coated/infiltrated LPS significantly increased to ~98% (Fig. 3, C and D), while the CEs of the untreated LPS cell and the Au-coated LPS cell are only 85 to 90%. The in situ-formed LiF-rich SEI reduces the contact resistance and effectively suppresses the Li dendrite growth and side reactions between the LPS electrolyte and the Li metal. Therefore, a very high cycling CE for the LiFSI-coated/infiltrated LPS is achieved after the initial few activation cycles. Although there is some nonuniformity for the in situ-formed SEI layer in terms of physical morphology and chemical composition along the Li surface, compared with the high electron-conductive layers formed between the SSEs and the Li metal, this electronic insulating LiF-rich SEI can effectively improve the critical current density and suppress the

Li dendrites in SSEs. Without this layer, the in situ-formed interphase with high electron conductivity due to the reaction between the SSEs and the Li metal can promote the Li dendrite formation in the SSEs.

Interphase chemistry

Since the nature of the interphase layers between the Li metal and the SSEs drastically changed the behavior of the Li metal plating and stripping, the interphase morphology and composition were analyzed using scanning electron microscopy (SEM), time-of-flight secondary ion mass spectrometry (ToF-SIMS), and x-ray photoelectron spectroscopy (XPS). Figure 4 (A and B) shows the surface morphology of the cycled LPS recovered from Li|LPS|SS and Li|LiFSI@LPS|SS. The untreated LPS shows substantial cracking after prolonged cycling due to the side reactions ($\text{Li}_3\text{PS}_4 + 8\text{Li} \rightarrow \text{Li}_3\text{P} + 4\text{Li}_2\text{S}$) between the Li metal and the solid-state LPS electrolyte, as evidenced by the low CE and poor cycling stability (Fig. 3D). Figure 4D shows the ternary phase diagram of the Li-P-S obtained from

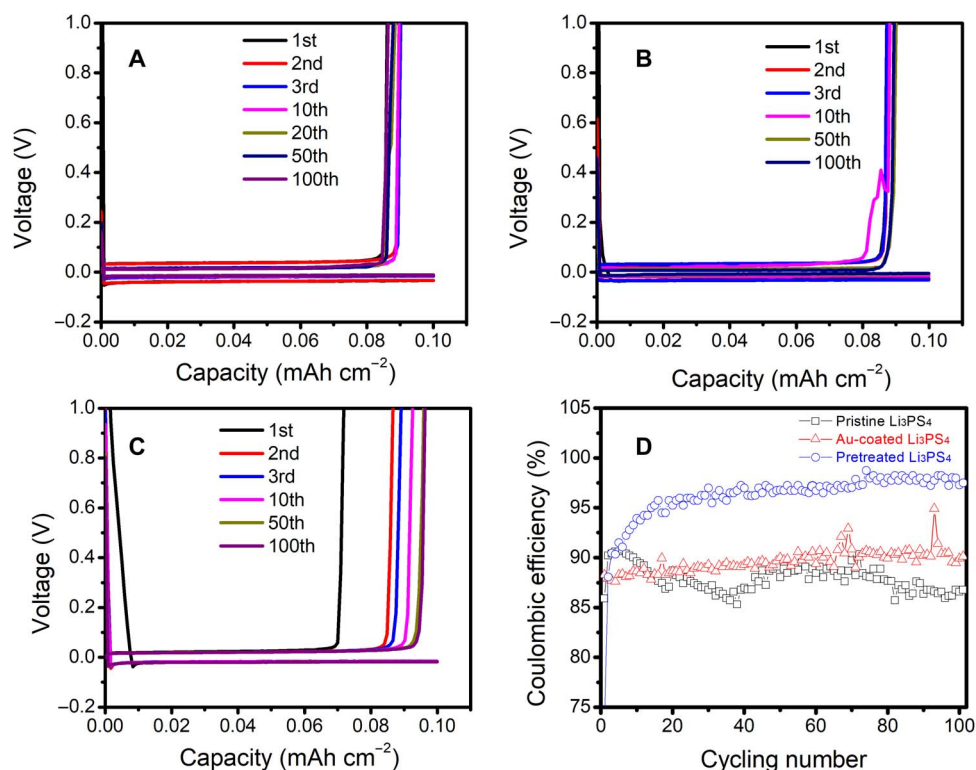


Fig. 3. Electrochemical properties of the Li|LPS|SS cells. Li plating/stripping profiles on an SS working electrode using (A) the pristine LPS as the SSE, (B) the Au-coated LPS as the SSE, and (C) the 6 M LiFSI DME pretreated LPS as the SSE. (D) Li plating/stripping CEs in different LPS. The current density is 0.1 mA cm⁻².

Materials Project (MP) (30). The reaction between the LPS and the Li metal will ultimately form the fully lithiated species of Li₂S and Li₃P, with LiP₇, Li₃P₇, and LiP as the possible intermediates. However, these reduction products cannot act as effective SEI layers due to the high electronic conductivity of Li_xP (figs. S4 and S5). The formation of the lithiated layer will increase the Li content on the LPS surface. ToF-SIMS analysis was used to map the Li content in the cross section. As shown in fig. S4, the Li content in the cracked layer of the cycled LPS SSE was higher than that in the bulk LPS SSE, confirming the side reactions of LPS with Li. XPS was also performed to obtain the detailed composition information on the interface layer (Fig. 4, C, E, and F, and fig. S6). For the cycled LPS recovered from the untreated Li|LPS|SS battery, significantly high doublet peaks of Li₃P (2p_{3/2}: 126 eV) were observed, in addition to P doublet peaks of 2p_{3/2} and 2p_{1/2} (~132.5 eV) from LPS (31). A few tiny peaks at 130.3 eV in XPS could be attributed to other reduced P compounds (Li_xP, 0 ≤ x < 3) (31). The XPS surface composition analysis confirms the serious parasitic reactions between the LPS SSE and the Li metal during the Li plating/stripping process, which is in line with the previous reports (31, 32) and the reaction mechanism based on the ternary phase diagram in Fig. 4D. All the analyses from the SEM, XPS, and ToF-SIMS proved that significant reactions take place between the LPS SSE and the Li metal anode, leading to the formation of the lithiated by-products and cracks. Hayashi and colleagues (31) reported that LPS coated by Au is also reduced by Li.

For the Li|LiFSI@LPS|SS cell, the situation is totally different. The LPS recovered from the cycled Li|LiFSI@LPS|SS cell showed a rather dense and smooth surface without any cracking after prolonged cycling (Fig. 4B). No Li₃P peaks (Fig. 4E), but a significantly high LiF peak, were detected in the XPS (Fig. 4F and fig. S6). Besides the

LiF, C-O and C-C species (fig. S7A, C 1s) were also detected because of the side reactions between the DME and the Li metal during the evacuation process. The Li₂S, Li₂S₂ (fig. S7B, S 2p), and Li₂O (fig. S7C, O 1s) are formed because of the reaction of the LiFSI with the Li metal anode. The composition depth profile on the surface of the cycled LPS in the Li|LiFSI@LPS|SS cell was characterized using ToF-SIMS (Fig. 4, G to I, and fig. S8). Figure 4G shows the side surface of the crater sputtered by Ga⁺ ions. Significantly high fluorine signals were found within the top surface layer (1 μm) of the LPS (Fig. 4H), while the content of S on the top surface is relatively low (Fig. 4I), indicating a thin and robust LiF-rich SEI layer that prevents the possible reactions of the LPS SSE with the Li metal anode.

All the characterizations demonstrated that Li reacted with LPS, forming an electronic conductive Li_xP-containing interphase, and Au coating on the LPS cannot prohibit the side reactions although it enhances the surface contacting areas between the Li and the LPS and reduces the reaction overpotentials. The formation of an electronic insulating LiF-rich SEI by coating/infiltrating LiFSI on the LPS can block the side reactions and significantly increase the CE of Li plating/stripping (Fig. 3).

Li dendrite suppression of LiF interphase

Theoretical calculations based on density functional theory (DFT) were used to explain why the LiF-rich SEI layer can effectively block the Li dendrites in the SSEs. To evaluate the ability of SEI layer components on suppression of the Li dendrites, a critical length for an Li dendrite in SEI is defined as the minimum Li dendrite length before the Li dendrite becomes stable and begins to grow (note S1). Critical length can be used to evaluate the Li dendrite growth-suppressing ability of the SSEs. The larger the critical length of the Li dendrite

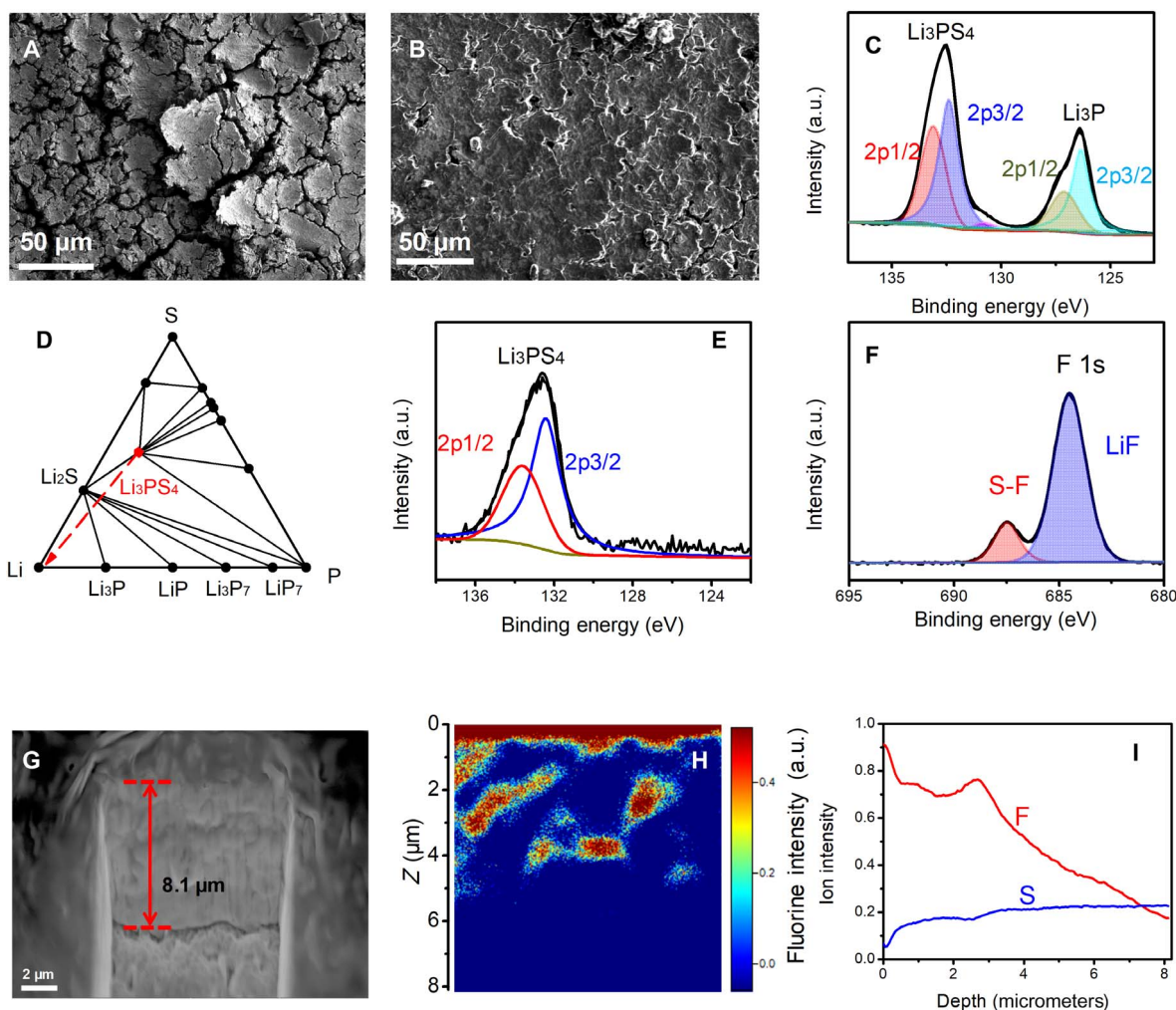


Fig. 4. Surface analyses for the cycled LPS SSE from the Li|LPS|SS cell. (A) SEM image of the cycled LPS recovered from the untreated cell. (B) SEM image of cycled LPS recovered from the pretreated cell. (C) High-resolution XPS analysis of P-containing species in the LPS recovered from an untreated SSE cell. a.u., arbitrary units. (D) Ternary phase diagram of Li-P-S. (E and F) High-resolution XPS analysis of P- and F-containing species in the LPS recovered from the pretreated cell. (G) Crater sputtered by a Ga^+ ion beam for the pretreated LPS after cycling. (H) ToF-SIMS analysis for the fluorine element in the pretreated LPS after cycling. (I) F and S element distribution in the sputtered LPS SSE as shown in (G).

is, the higher the Li dendrite resistivity the SSE has. As illustrated in Fig. 5A, during Li plating, Li dendrites have to first go through the passivation layer along the grain boundaries in which high strain energy is found at the tip of the boundary. On the basis of the energy analysis, the interfacial energy will increase because of the formation of a new interface at the Li/SEI, while the strain energy releases as the dendrite grows (Fig. 5B). The total energy increases with increase of Li dendrite length and reaches the maximum at the critical dendrite length L_c , and then the total energy begins to decrease (fig. S9)

$$L_c = \frac{2\gamma E}{\pi\sigma^2} \quad (1)$$

L_c is the minimum Li dendrite length before the Li dendrite becomes stable and begins to grow, which is the critical Li dendrite length for further growth. γ represents the interfacial energy required to form a new Li/SEI interface per unit surface area. σ is the stress at

the tip of the crack or grain boundary, which is mainly determined by the external current. E is the bulk modulus. This critical Li dendrite length is similar to the critical radius in homogeneous and heterogeneous nucleation processes (33). Once the dendrite length is larger than the critical length, the dendrite can grow without any additional energy input, which means that the dendrite can grow spontaneously (fig. S9). Therefore, the critical length (fig. S9) can be used to evaluate the ability of SEI to suppress the Li dendrite growth. The larger L_c means higher Li dendrite suppression ability of SEI.

On the basis of Eq. 1 in energy analysis, for a given current, the critical length increases with the Li/SEI interfacial energy (γ) per unit interface area and the bulk modulus of passivation layer components (note S1). Figure 5C demonstrates the plot of the relationship between the interfacial energy (γ) of different SEI components and the number of Li metal formula units. Using the same method as in a previous work (34), the interfacial energy (γ) can be obtained from the intercept of the fitted line in Fig. 5C. As shown in Fig. 5D, LPS has a negative interfacial energy ($-88.92 \text{ meV}/\text{\AA}^2$), indicating an

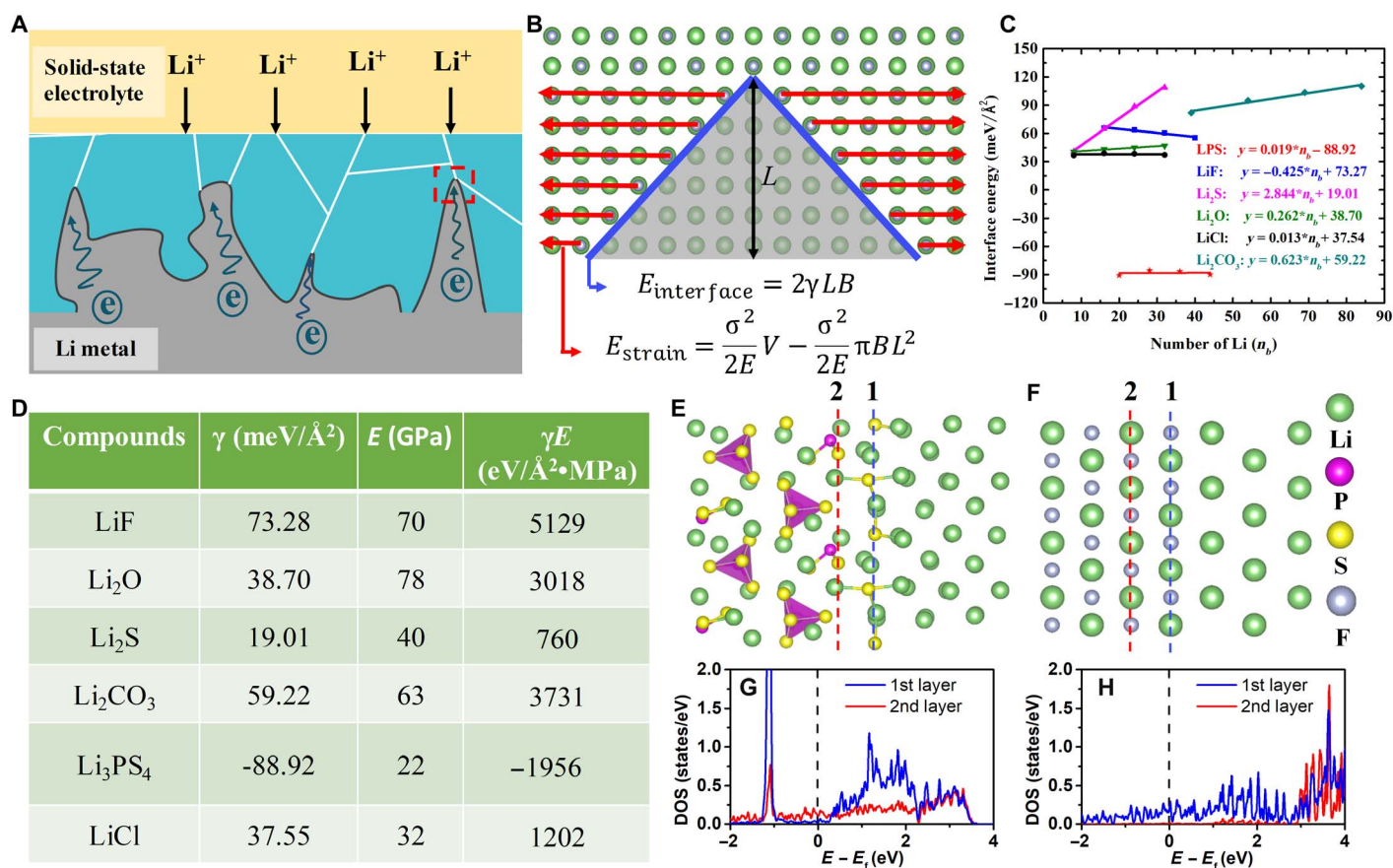


Fig. 5. DFT calculations for the mechanism of the LiF-rich SEI layer on suppression of the Li dendrite in SSEs. (A) Schematic illustration of the electrochemical deposition process of the Li metal anode. (B) Energy-based analysis (interfacial energy and strain energy) of Li dendrite formation. (C) Plot of the relationship between the interfacial energy for possible SEI components and the number of Li metal formula units. (D) Calculated interfacial energies γ , bulk modulus E from MP (45), and Li dendrite suppression ability γE for different interface components. DFT-optimized atomic structures of (E) LPS/Li and (F) LiF/Li interfaces and its corresponding DOS (G and H) profiles by atomic layer with Fermi level at 0 eV. The green, purple, yellow, and gray balls in (E) and (F) represent Li, P, S, and F atoms, respectively.

intrinsically unstable interface between the LPS and the Li metal. Therefore, the LPS will spontaneously react with the Li metal, which is in agreement with previous experimental and theoretical results (32). The reaction between Li and LPS forms cracks (Fig. 5A) because the reaction between the LPS and the Li metal leads to the reconstruction of the LPS with the formation of Li-S and Li-P compounds based on the DFT-optimized atomic interlayer structure calculation (Fig. 5E). In contrast to LPS, other components in normal SEI (LiF, Li_2O , Li_2S , Li_2CO_3 , and LiCl) have positive interfacial energy with Li. Among them, LiF exhibits the highest interfacial energy of 73.28 meV/Å², suggesting worst wettability to the Li metal but highest Li dendrite suppression ability. The interfacial energy of the solid-solid interface is mainly determined by two factors: (i) lattice mismatch. Generally, the non-coherent interface exhibits higher interfacial energy than the coherent interface. (ii) Formation energies for the interphases. Larger formation energy will lead to higher interfacial energy. LiF has an extremely larger interfacial energy than other SEI components. The detailed computational model and method for the interfacial energy are shown in note S2. The bulk modulus (E) and the calculated Li dendrite suppression ability (γE) are also summarized in the table in Fig. 5D. In addition to high interfacial energy, LiF also has a high bulk modulus (70 GPa) and leads to the highest value of γE (5129 eV/Å²•MPa). In all SEI components, LiF has the highest ability

to suppress Li dendrites. In sharp contrast, LPS has a negative γE value and interfacial energy, which intrinsically promotes the dendrite propagation.

The high electron blocking effect of SEI can inhibit the possible side reactions between the LPS and the Li metal. The ability for electron transfer from Li to SEI was directly calculated from density of states (DOS) profiles by taking the difference of the conduction band minimum and Fermi level (0 eV). Figure 5 (G and H) shows the electron tunneling barrier from Li to LiF or LPS. The electron tunneling barrier between the Li and the LPS (either layer 1 or 2) is close to 0 eV, indicating that the two atomic layers of degraded LPS are highly electron conductive and cannot block the electrons migrating from the Li metal to inner LPS. In contrast, the electron tunneling barrier between the Li metal and LiF highly increases from 0 eV (layer 1) to over 2.0 eV at layer 2, proving that LiF is specifically effective in blocking electrons from moving from the Li metal anode to the LiF-rich SEI layer. The high electron blocking effect could inhibit possible side reactions between the LPS and the Li metal.

Electrochemical performance of Li metal full cells

The electrochemical performance of the Li|LCO full cells using two different LPS electrolytes (LiFSI-treated LPS and pristine LPS) is evaluated at a high lithium cobalt oxide (LCO) areal capacity of

$\sim 1.0 \text{ mAh cm}^{-2}$. This high loading represents a strict test for the solid-state batteries because it maximizes the side reactions during Li plating/stripping cycles due to the high utilization of the Li metal anode. Figure 6A shows the charge/discharge curves of the Li|LiFSI@LPS|LCO cell at the current density of 0.3 mA cm^{-2} . The irreversible capacity between 3.5 and 3.8 V in the first charge process could be attributed to the side reactions between the pretreated SSE and the LCO cathodes. Highly reversible lithiation/delithiation can be achieved in the following cycles with a capacity of 120 mAh g^{-1} . After 10 cycles, a high CE of $>99.8\%$ could be obtained. However, for the Li|LPS|LCO cell with the untreated LPS as the SSE, cell failure due to short circuit was observed after only two cycles (fig. S10).

DISCUSSION

As shown in Fig. 7, three types of interphases/interfaces could be formed between the SSEs and the Li metal: (i) type I—intrinsically stable interface, in which the electrolytes are thermodynamically stable with the Li metal (Fig. 7A). Li_3N with a high Li ion conductivity of $10^{-4} \text{ S cm}^{-1}$ can be considered as a model electrolyte. (ii) Type II—SEI, which has negligible electron conductivity but sufficient Li ion conductivity (Fig. 7B). LiPON can be considered as a model type II electrolyte. (iii) Type III—electronic conducting interphase with a higher electronic conductivity than the electrolyte (Fig. 7C). $\text{Li}_{0.5}\text{La}_{0.5}\text{TiO}_3$ (LLTO) is a typical electrolyte for type III. For the first type of the SSEs, the potential abruptly drops from SSE potential to Li metal at the interface since Li does not wet the SSE, inducing a high interface resistance (Fig. 7D). For the second type of SSE, LiPON will react with Li, forming an Li_2O -rich SEI layer, which can effectively block electron transport (35). The potential of the electrolyte also abruptly drops to the Li potential within the thin SEI layer (Fig. 7D). The Li ions can facilitate hop in the SEI layers with negligible electron conductivity (Fig. 7B), which can effectively block the continuous degradation of the electrolytes during prolonged cycling. In addition to LLTO, sulfides and oxide electrolytes can also be classified as the third type because the SSEs have a tendency to be reduced by an Li metal anode at a negative potential during Li plating (negative overpotential values depend on Li plating currents), forming electron-conducting species (such as Ti, GeLi_x , and Zr for LLTO, LGPS, and LLZO, respectively) or electronic semiconducting species (such as Li_3P for LPS and LGPS) (36). The bandgaps of the species generated

by the reaction of the SSEs to the Li metal are shown in fig. S5. The electron-conductive species generated, along with the volume expansion-induced cracks during the lithiation of the SSE, speed up the degradation of the SSEs. The high electronic conductivity of the interphase also reduces the potential in the electron-conductive interphase (III' curve in Fig. 7D). The partial interphase region (as denoted by the red double-arrow line) will be below the potential of Li deposition; therefore, Li dendrites will be formed in the interphase. The instability and sufficient electronic conductivity of the SSEs and the high overpotentials during Li plating eventually induce not only Li dendrite growth along the phase boundaries but also direct Li precipitation in the SSEs (37).

Since most of the electrolytes are thermodynamically not stable to the Li metal, formation of SEI layers is the most practical way to prevent the continuous degradation of SSEs and achieve a high CE (19). If the SEI layer is an electronic insulator and a high ionic conductor, it can block the reactions between the Li metal and the electrolyte by abruptly raising the potential from the Li metal anode to the SSE within the SEI nanolayer without adding additional ionic resistance (Fig. 7B). However, if the interphase is an electronic conductor, continuous reactions between the electrolyte and the Li metal will occur and inevitably lead to failure of the cells. Most state-of-the-art SSEs (such as LPS, LGPS, and LLZO) cannot form an electronic insulating SEI layer once they make contact with the highly reactive Li metal anodes. For example, Li_xGe and Li_3P will be generated from the reduction of LGPS (21), Li_3P will be formed from the reduction of LPS once it makes contact with the Li metal, where the Li_3P is a semiconductor with a bandgap (0.7 eV) comparable to the Ge (0.66 eV). Similarly, a high conductive Zr metal will be formed from the reduction of the LLZO garnets at a negative potential versus Li/Li^+ (21). These conductive interphases have a much higher electronic conductivity than the SEI layer formed in the conventional nonaqueous organic electrolytes, which cannot block further reactions between the Li metal and the SSEs. Therefore, constructing an electronic insulating SEI layer between Li and SSE should be the most effective method to realize the high reversibility of solid-state Li metal batteries. Although an electron-conducting interphase formed by coating Li-active material (including metal, carbon, and metal oxides) layers can wet Li with SSE and reduce the overpotentials/hysteresis due to the amelioration of the contact areas (as shown in Fig. 2B), the high electronic conductivity and the equi-

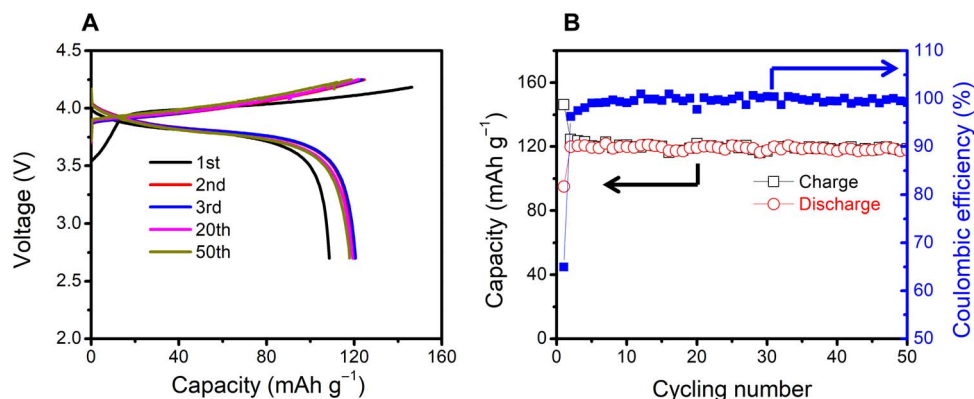


Fig. 6. Electrochemical performance of Li|LiFSI@LPS|LCO. (A) Charge/discharge curves in different cycles at 0.3 mA cm^{-2} at room temperature. (B) Cycling performance of the cell at 0.3 mA cm^{-2} at room temperature. The area loading is 1.0 mAh cm^{-2} .

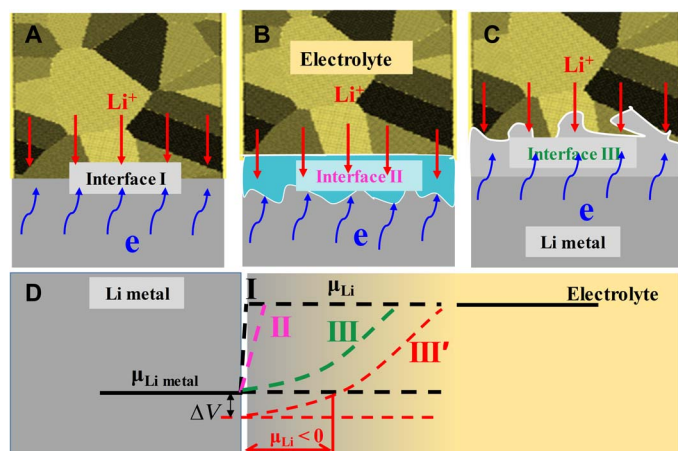


Fig. 7. Interphase types between the Li metal and the SSEs. (A) Thermodynamically stable interphase. (B) Reactive but forming an electron insulator SEI layer. (C) Reactive and forming a degradation layer with high electron conductivity. (D) Li potentials between the Li metal and the SSEs in the above three interphase types. The difference between the green dash line (III) and the red dash line (III') includes the overpotentials during the Li plating process.

potential between this layer and the deposited Li metal in the interphase allow continuous side reactions or even direct deposit of Li inside the SSE (Fig. 3B).

In summary, LPS SSEs in Li metal batteries are intrinsically unstable to the Li metal anode and are reduced to a nonpassivated layer during the Li plating/stripping process, promoting Li dendrite growth. Coating an electron-conductive layer (such as Au) between the SSEs and the Li metal cannot effectively block the parasitic reactions between the SSEs and the Li metal, although the Li plating/stripping overpotential was reduced because of the enhancement of the contacting area. By introducing a LiF-rich SEI layer between the LPS SSE and the Li metal anode through coating/infiltrating LiFSI into the LPS, we significantly increased the critical current density of an LPS from 0.7 mA cm^{-2} to a record-high value of $>2 \text{ mA cm}^{-2}$ at room temperature, markedly enhanced the Li plating/stripping CE from 88 to 98%, and realized stable cycling performance of an SSE Li metal full cell with high cathode loading. In-depth analysis using SEM, XPS, ToF-SIMS, and first principles calculations revealed that the LiF-rich SEI layer with low electronic conductivity effectively blocked the parasitic reactions between the SSEs and the Li metal, while the high interfacial energy and the high bulk modulus to the Li metal suppressed the dendrite formation, all of which markedly enhanced the electrochemical performance of the solid-state Li metal batteries. The present SEI engineering approach potentially resolves the intrinsic challenges for the SSEs in the Li metal cells and could pave the way for the next-generation high-energy solid-state Li metal batteries.

MATERIALS AND METHODS

Materials

Li chips with a thickness of 250 μm were obtained from MTI Corporation. Amorphous LPS was synthesized by ball milling the Li_2S (99.98%, Sigma-Aldrich) and P_2S_5 (99%, Sigma-Aldrich) in a zirconia ceramic vial. Lithium bis(fluorosulfonyl) imide (LiFSI) was purchased from NIPPON SHOKUBAI CO., LTD. 1,2-DME (anhydrous, 99.5%) was bought from Sigma-Aldrich.

Materials characterization

Powder XRD results were obtained with a D8 Advance with LynxEye and SolX (Bruker, USA) using Cu K α radiation. XPS was conducted on a high-sensitivity Kratos AXIS 165 x-ray photoelectron spectrometer using Mg K α radiation. All binding energy values were referenced to the C 1s peak at 284.6 eV. The content of different species was obtained by fitting the whole XPS spectra using the CasaXPS software. The distributions of different elements in different depths of the cycled LPS SSEs were analyzed using a time-of-flight secondary ion mass spectrometer attached with a Ga $^+$ focused ion beam (FIB)/scanning electron microscope (Tescan GAIA3). The accelerated voltage for FIB/SEM was 20 kV.

Electrochemical measurements

An LiFSI DME electrolyte (6 M) was prepared by adding LiFSI into anhydrous DME solvents. Before preparing the electrolyte, DME was dried with a molecular sieve (4 \AA , Sigma-Aldrich) to reduce the water content to less than 5 ppm, which is measured with a Karl-Fisher titrator (Metrohm 899 Coulometer). All the cells were assembled in an Ar-filled glove box with O_2 and moisture content of <2 ppm. To assemble the Li|LPS|Li solid-state cell, 110 mg of LPS SSE was pressed into a pellet under 300 MPa in a polytetrafluoroethylene hollow cylinder with a diameter of 10 mm. Then, one drop of 6 M LiFSI DME was added on both sides of the LPS pellet, and two Li foils with the same diameter were attached on both sides. After that, the Li|LPS|Li was dried at 120°C under vacuum overnight. The dried Li|LPS|Li cell was then sandwiched between two SS rods, which functioned as current collectors. For reference, the Li|LPS|Li cell without LiFSI was also assembled with the same procedures. A huge volume change of the electrodes will trigger the contact issues, changing the local current densities during cycling. To avoid the contact issues in the Li|LPS|SS cell, a relatively small plating capacity of 0.1 mAh cm^{-2} was applied for all the SSE Li metal cells. To obtain the interfacial information on the LPS SSE, LPS was recovered from the Li|LPS|SS after cycling. The surface of the LPS facing the SS was analyzed. For the Li||LCO solid-state cells, the cathode of LiCoO_2 was precoated with LiNbO_2 through the sol-gel method followed by heat treatment (38). The loading of the cathode is about 1 mAh cm^{-2} . The weight ratio of the LiNbO_2 -coated LiCoO_2 and LPS was 70:30. The ionic conductivity of the LPS was measured by the EIS test of the Pt|LPS|Pt cell, which was tested on a Gamry workstation (Gamry 1000E, Gamry Instruments, USA). The galvanostatic cycling test was determined by an Arbin BT2000 workstation (Arbin Instruments, USA). All the electrochemical tests were performed at room temperature (25°C).

Computation details

First principles computations based on DFT (39, 40) were performed using the VASP. The projector augmented wave (41) method with an energy cutoff of 520 eV was used to describe the ion-electron interaction on a well-converged k -point mesh. The Perdew-Burke-Ernzerhof functional in the generalized gradient approximation (42) was used to calculate the exchange-correlation energy. The interface energy was evaluated using the same method in a previous work (34). To optimize the interface configuration, the lattice parameter perpendicular to the interface was relaxed while the others are fixed. The geometry optimizations were performed using the conjugated gradient method, and the convergence threshold was set to be 10^{-5} eV in energy and 0.01 eV/ \AA in force. Visualization of the structures was made by combining the use of VESTA (Visualization for Electronic

and STructure Analysis), OVITO (Open VIsualization TOol), and Atomsk (43, 44).

SUPPLEMENTARY MATERIALS

Supplementary material for this article is available at <http://advances.sciencemag.org/cgi/content/full/4/12/eaau9245/DC1>

Fig. S1. XRD pattern and the electrochemical impedance spectra of the as-synthesized LPS SSE.

Fig. S2. Impedance plot of the Li|LPS|Li cell before cycling and after cycling.

Fig. S3. SEI impedance plot of the pretreated Li|LPS|Li cell before cycling and after cycling.

Fig. S4. ToF-SIMS analysis of the positive ions for the interface of the LPS.

Fig. S5. Comparison of the bandgaps for different materials.

Fig. S6. XPS spectra of cycled LPS recovered from the pretreated SSE cell and untreated cell.

Fig. S7. SEI components in the LPS recovered from the pretreated cell by XPS.

Fig. S8. ToF-SIMS analysis of the negative ions for the interface of the cycled LPS SSE.

Fig. S9. Relationship between the total energy, the interfacial energy, and the strain energy with the dendrite length during the dendrite formation in the SSEs.

Fig. S10. Charge/discharge curves for the Li|LPS|LCO cell.

Note S1. Critical Li dendrite length and the Li dendrite suppression ability for the SSEs.

Note S2. Computational model and method for the interfacial energy.

References (46–48)

REFERENCES AND NOTES

- J. W. Choi, D. Aurbach, Promise and reality of post-lithium-ion batteries with high energy densities. *Nat. Rev. Mater.* **1**, 16013 (2016).
- Y. Lu, Z. Tu, L. A. Archer, Stable lithium electrodeposition in liquid and nanoporous solid electrolytes. *Nat. Mater.* **13**, 961–969 (2014).
- M. D. Tikekar, S. Choudhury, Z. Tu, L. A. Archer, Design principles for electrolytes and interfaces for stable lithium-metal batteries. *Nat. Energy* **1**, 16114 (2016).
- L. Fan, S. Wei, S. Li, Q. Li, Y. Lu, Recent progress of the solid-state electrolytes for high-energy metal-based batteries. *Adv. Energy Mater.* **8**, 1702657 (2018).
- B. Wu, S. Wang, J. Lochala, D. Desrochers, B. Liu, W. Zhang, J. Yang, J. Xiao, The role of the solid electrolyte interphase layer in preventing Li dendrite growth in solid-state batteries. *Energy Environ. Sci.* **11**, 1803–1810 (2018).
- C. Monroe, J. Newman, The impact of elastic deformation on deposition kinetics at lithium/polymer interfaces. *J. Electrochem. Soc.* **152**, A396–A404 (2005).
- J. Wolfenstine, J. L. Allen, J. Sakamoto, D. J. Siegel, H. Choe, Mechanical behavior of Li-ion-conducting crystalline oxide-based solid electrolytes: A brief review. *Ionics* **24**, 1271–1276 (2018).
- C. Brissot, M. Rosso, J.-N. Chazalviel, S. Lascaud, Dendritic growth mechanisms in lithium/polymer cells. *J. Power Sources* **81–82**, 925–929 (1999).
- L. Porz, T. Swamy, B. W. Sheldon, D. Rettenwander, T. Frömling, H. L. Thaman, S. Berendts, R. Uecker, W. C. Carter, Y.-M. Chiang, Mechanism of lithium metal penetration through inorganic solid electrolytes. *Adv. Energy Mater.* **7**, 1701003 (2017).
- R. Garcia-Mendez, F. Mizuno, R. Zhang, T. S. Arthur, J. Sakamoto, Effect of processing conditions of 75Li₂S-25P₂S₅ solid electrolyte on its DC electrochemical behavior. *Electrochim. Acta* **237**, 144–151 (2017).
- M. Nagao, A. Hayashi, M. Tatsumisago, T. Kanetsuku, T. Tsuda, S. Kuwabata, In situ SEM study of a lithium deposition and dissolution mechanism in a bulk-type solid-state cell with a Li₂S-P₂S₅ solid electrolyte. *Phys. Chem. Chem. Phys.* **15**, 18600–18606 (2013).
- F. Han, J. Yue, X. Zhu, C. Wang, Suppressing Li dendrite formation in Li₂S-P₂S₅ solid electrolyte by Lil incorporation. *Adv. Energy Mater.* **8**, 1703644 (2018).
- E. J. Cheng, A. Sharafi, J. Sakamoto, Intergranular Li metal propagation through polycrystalline Li_{6.25}Al_{0.25}La₃Zr₂O₁₂ ceramic electrolyte. *Electrochim. Acta* **223**, 85–91 (2017).
- B. Xu, W. Li, H. Duan, H. Wang, Y. Guo, H. Li, H. Liu, Li₃PO₄-added garnet-type Li_{6.5}La₃Zr_{1.5}Ta_{0.5}O₁₂ for Li-dendrite suppression. *J. Power Sources* **354**, 68–73 (2017).
- F. Yonemoto, A. Nishimura, M. Motoyama, N. Tsuchimine, S. Kobayashi, Y. Iriyama, Temperature effects on cycling stability of Li plating/stripping on Ta-doped Li₇La₃Zr₂O₁₂. *J. Power Sources* **343**, 207–215 (2017).
- R. H. Basappa, T. Ito, T. Morimura, R. Bekarevich, K. Mitsuishi, H. Yamada, Grain boundary modification to suppress lithium penetration through garnet-type solid electrolyte. *J. Power Sources* **363**, 145–152 (2017).
- L. L. Baranowski, C. M. Heveran, V. L. Ferguson, C. R. Stoldt, Multi-scale mechanical behavior of the Li₃PS₄ solid-phase electrolyte. *ACS Appl. Mater. Interfaces* **8**, 29573–29579 (2016).
- J. Qian, W. A. Henderson, W. Xu, P. Bhattacharya, M. Engelhard, O. Borodin, J.-G. Zhang, High rate and stable cycling of lithium metal anode. *Nat. Commun.* **6**, 6362 (2015).
- X. Fan, L. Chen, X. Ji, T. Deng, S. Hou, J. Chen, J. Zheng, F. Wang, J. Jiang, K. Xu, C. Wang, Highly fluorinated interphases enable high-voltage Li-metal batteries. *Chem* **4**, 174–185 (2018).
- P. Bai, J. Li, F. R. Brushett, M. Z. Bazant, Transition of lithium growth mechanisms in liquid electrolytes. *Energy Environ. Sci.* **9**, 3221–3229 (2016).
- F. Han, Y. Zhu, X. He, Y. Mo, C. Wang, Electrochemical stability of Li₁₀GeP₂S₁₂ and Li₇La₃Zr₂O₁₂ solid electrolytes. *Adv. Energy Mater.* **6**, 1501590 (2016).
- Y. Zhu, X. He, Y. Mo, Origin of outstanding stability in the lithium solid electrolyte materials: Insights from thermodynamic analyses based on first-principles calculations. *ACS Appl. Mater. Interfaces* **7**, 23685–23693 (2015).
- B. Chen, J. Ju, J. Ma, J. Zhang, R. Xiao, G. Cui, L. Chen, An insight into intrinsic interfacial properties between Li metals and Li₁₀GeP₂S₁₂ solid electrolytes. *Phys. Chem. Chem. Phys.* **19**, 31436–31442 (2017).
- J. Wolfenstine, J. L. Allen, J. Read, J. Sakamoto, Chemical stability of cubic Li₇La₃Zr₂O₁₂ with molten lithium at elevated temperature. *J. Mater. Sci.* **48**, 5846–5851 (2013).
- N. J. Taylor, S. Stangeland-Molo, C. G. Haslam, A. Sharafi, T. Thompson, M. Wang, R. Garcia-Mendez, J. Sakamoto, Demonstration of high current densities and extended cycling in the garnet Li₇La₃Zr₂O₁₂ solid electrolyte. *J. Power Sources* **396**, 314–318 (2018).
- X. Fan, L. Chen, O. Borodin, X. Ji, J. Chen, S. Hou, T. Deng, J. Zheng, C. Yang, S.-C. Liou, K. Amine, K. Xu, C. Wang, Non-flammable electrolyte enables Li-metal batteries with aggressive cathode chemistries. *Nat. Nanotechnol.* **13**, 715–722 (2018).
- X.-B. Cheng, J.-Q. Huang, Q. Zhang, Review—Li metal anode in working lithium-sulfur batteries. *J. Electrochem. Soc.* **165**, A6058–A6072 (2018).
- S. Choudhury, L. A. Archer, Lithium fluoride additives for stable cycling of lithium batteries at high current densities. *Adv. Electron. Mater.* **2**, 1500246 (2016).
- S. Choudhury, C. T.-C. Wan, W. I. Al Sadat, Z. Tu, S. Lau, M. J. Zachman, L. F. Kourkoutis, L. A. Archer, Designer interphases for the lithium-oxygen electrochemical cell. *Sci. Adv.* **3**, e1602809 (2017).
- S. P. Ong, L. Wang, B. Kang, G. Ceder, Li-Fe-P-O₂ phase diagram from first principles calculations. *Chem. Mater.* **20**, 1798–1807 (2008).
- A. Kato, H. Kowada, M. Deguchi, C. Hotehama, A. Hayashi, M. Tatsumisago, XPS and SEM analysis between Li/Li₃PS₄ interface with Au thin film for all-solid-state lithium batteries. *Solid State Ion.* **322**, 1–4 (2018).
- W. D. Richards, L. J. Miara, Y. Wang, J. C. Kim, G. Ceder, Interface stability in solid-state batteries. *Chem. Mater.* **28**, 266–273 (2016).
- N. H. Fletcher, Size effect in heterogeneous nucleation. *J. Chem. Phys.* **29**, 572–576 (1958).
- N. D. Lepley, N. A. W. Holzwarth, Modeling interfaces between solids: Application to Li battery materials. *Phys. Rev. B* **92**, 214201 (2015).
- S. Siculo, M. Fingerle, R. Hausbrand, K. Albe, Interfacial instability of amorphous LiPON against lithium: A combined density functional theory and spectroscopic study. *J. Power Sources* **354**, 124–133 (2017).
- J. Yue, F. Han, X. Fan, X. Zhu, Z. Ma, J. Yang, C. Wang, High-performance all-inorganic solid-state sodium-sulfur battery. *ACS Nano* **11**, 4885–4891 (2017).
- F. Aguesse, W. Manalastas, L. Buannic, J. M. Lopez del Amo, G. Singh, A. Llordes, J. Kilner, Investigating the dendritic growth during full cell cycling of garnet electrolyte in direct contact with Li metal. *ACS Appl. Mater. Interfaces* **9**, 3808–3816 (2017).
- W. Sun, M. Xie, X. Shi, L. Zhang, Study of new phases grown on LiNbO₃ coated LiCoO₂ cathode material with an enhanced electrochemical performance. *Mater. Res. Bull.* **61**, 287–291 (2015).
- P. Hohenberg, W. Kohn, Inhomogeneous electron gas. *Phys. Rev.* **136**, B864–B871 (1964).
- W. Kohn, L. J. Sham, Self-consistent equations including exchange and correlation effects. *Phys. Rev.* **140**, A1133–A1138 (1965).
- P. E. Blöchl, Projector augmented-wave method. *Phys. Rev. B* **50**, 17953–17979 (1994).
- J. P. Perdew, K. Burke, M. Ernzerhof, Generalized gradient approximation made simple. *Phys. Rev. Lett.* **77**, 3865–3868 (1996).
- A. Stukowski, Visualization and analysis of atomistic simulation data with OVITO—the open visualization tool. *Model. Simul. Mat. Sci. Eng.* **18**, 015012 (2010).
- P. Hirel, Atomsk: A tool for manipulating and converting atomic data files. *Comput. Phys. Commun.* **197**, 212–219 (2015).
- M. de Jong, W. Chen, T. Angsten, A. Jain, R. Notestine, A. Gamst, M. Sluiter, C. K. Ande, S. van der Zwaag, J. J. Plata, C. Toher, S. Curtarolo, G. Ceder, K. A. Persson, M. Asta, Charting the complete elastic properties of inorganic crystalline compounds. *Sci. Data* **2**, 150009 (2015).
- B. V. Suresh, *Solid State Devices and Technology* (Pearson Education, 2010).
- A. Jain, S. P. Ong, G. Hautier, W. Chen, W. D. Richards, S. Dacek, S. Cholia, D. Gunter, D. Skinner, G. Ceder, Commentary: The materials project: A materials genome approach to accelerating materials innovation. *APL Mater.* **1**, 011002 (2013).
- A. A. Griffith, M. Eng, VI. The phenomena of rupture and flow in solids. *Phil. Trans. R. Soc. Lond. A* **221**, 163–198 (1921).

Acknowledgments: We acknowledge the University of Maryland supercomputing resources (<http://hpcc.umd.edu>) made available for conducting DFT computations in this paper. We also thank the Maryland NanoCenter and its AIMLab for support. **Funding:** This work was supported by the Energy Efficiency and Renewable Energy Office of the U.S. Department of Energy through the Battery500 Consortium Seedling project under contract DE-EE0008200. X.J. was supported by a fellowship from the China Scholarship Council (201606160018).

Author contributions: X.F., X.J., and F.H. designed the experiments. X.F. conducted the electrochemical experiments. X.J. and J.J. conducted the calculations. J.C. and J.Y. synthesized the SSEs. C.W. conceived and supervised the project. All the authors contributed to the interpretation of the results. **Competing interests:** The authors declare that they have no competing interests. **Data and materials availability:** All data needed to evaluate the

conclusions in the paper are present in the paper and/or the Supplementary Materials. Additional data related to this paper may be requested from the authors.

Submitted 27 July 2018

Accepted 20 November 2018

Published 21 December 2018

10.1126/sciadv.aau9245

Citation: X. Fan, X. Ji, F. Han, J. Yue, J. Chen, L. Chen, T. Deng, J. Jiang, C. Wang, Fluorinated solid electrolyte interphase enables highly reversible solid-state Li metal battery. *Sci. Adv.* **4**, eaau9245 (2018).

Fluorinated solid electrolyte interphase enables highly reversible solid-state Li metal battery

Xiulin Fan, Xiao Ji, Fudong Han, Jie Yue, Ji Chen, Long Chen, Tao Deng, Jianjun Jiang and Chunsheng Wang

Sci Adv 4 (12), eaau9245.
DOI: 10.1126/sciadv.aau9245

ARTICLE TOOLS

<http://advances.sciencemag.org/content/4/12/eaau9245>

SUPPLEMENTARY MATERIALS

<http://advances.sciencemag.org/content/suppl/2018/12/17/4.12.eaau9245.DC1>

REFERENCES

This article cites 47 articles, 3 of which you can access for free
<http://advances.sciencemag.org/content/4/12/eaau9245#BIBL>

PERMISSIONS

<http://www.sciencemag.org/help/reprints-and-permissions>

Use of this article is subject to the [Terms of Service](#)

Science Advances (ISSN 2375-2548) is published by the American Association for the Advancement of Science, 1200 New York Avenue NW, Washington, DC 20005. The title *Science Advances* is a registered trademark of AAAS.

Copyright © 2018 The Authors, some rights reserved; exclusive licensee American Association for the Advancement of Science. No claim to original U.S. Government Works. Distributed under a Creative Commons Attribution NonCommercial License 4.0 (CC BY-NC).